



Simulation of ground motion emissions from wind turbines in low mountain ranges: implications for amplitude decay prediction

Laura Gaßner · Marie A. Gärtner · Joachim Ritter

Received: 9 August 2023 / Accepted: 13 October 2023
© The Author(s) 2023

Abstract The characterization and prediction of wind turbine (WT) emissions are important steps in reducing their impact on humans or sensitive technologies such as seismic stations or physics experiments. Here, WT ground motion emissions are studied along two measurement lines set up at two wind farms on the Eastern Swabian Alb, southwest Germany. The main purpose of the data analysis is to estimate amplitude decay rates from vertical component data and surface wave phase velocities excited by the permanent motion of the WT towers. Phase velocities as well as geological information serve as input to build realistic subsurface models for numerical wave field simulations. Amplitude A decay rates are characterized by b -values through $A \sim 1/r^b$ depending on distance r and are derived from peaks in power spectral density (PSD). We find an increase of b_{PSD} with frequency from 0.5 to 3.2 for field data. For low frequencies (1.2 Hz and 3.6 Hz), b_{PSD} ranges from 0.5 to 1.1, hence close to the geometrical spreading factor of surface waves ($b_{\text{PSD}} = 1$). Anelastic damping and scattering seem not to be significant at

these frequencies which also shows in numerical simulations for quality factors $Q = 50 - 200$. We also find that the emitted wavefields from several WTs interfere, especially in the near-field, and produce strong local ground motion amplitudes. The inclusion of a steep topography present in low mountain ranges adds more wave field distortions which can further increase the amplitudes. This needs to be considered when predicting WT induced ground motions.

Keywords Seismological measurements · Wind turbine emissions · Amplitude decay · Wave field simulation

1 Introduction

In the course of the transition to renewable energies the expansion of wind energy is essential. While this fact is commonly accepted by society, the erection of wind turbines (WTs) is often met with opposition by local residents (Hübner et al. 2019, Umit and Schaffer 2022). Conflicts are related to the space required by WTs (though small compared to other energy sources), and the related intervention in nature when erecting the WTs. Furthermore, a fear of negative health effects caused by low frequency sound and vibration emissions of WTs is a major source of rejection (Gaßner et al. 2022, Gaßner and Ritter 2023a, Haac et al. 2019, Pohl et al. 2018). Although it has been shown that infrasound WT emissions are not harmful (e.g., Ascone et al. 2021;

L. Gaßner (✉) · M.A. Gärtner · J. Ritter
Karlsruhe Institute of Technology, Geophysical Institute,
Hertzstraße 16, 76187 Karlsruhe, Baden-Württemberg,
Germany
e-mail: laura.gassner@kit.edu

L. Gaßner
e-mail: marie.gaertner@student.kit.edu

M.A. Gärtner
e-mail: joachim.ritter@kit.edu

J. Ritter

Marshall et al. 2023) or that protection guidelines are not exceeded, negative psychological effects can still be observed, e.g., when wind energy projects are perceived as unfair (e.g., Hübner et al. 2019).

Within the Inter-Wind project, interdisciplinary measurement campaigns are directed at capturing acoustic, ground motion and meteorological data that can be linked to noise reports issued by residents living near wind farms during multiple campaigns (Gaßner et al. 2022). In surveys, residents reported that they perceive WT related vibrations, but measurements demonstrate that ground motion amplitudes remain significantly below the human perception threshold (approx. $100 \mu\text{m/s}$, DIN 4150-2, 1999 table 1). In addition to providing a ground motion data base for annoyance evaluation, line measurements were conducted to evaluate the amplitude decay of WT emissions. The decay is frequency dependent and related to the subsurface geology (Lerbs et al. 2020). Thus, measurements are needed to improve knowledge about amplitude decay rates for WT emissions in different geologic settings.

The vibration emissions are linked to the excited eigenmodes of the WT towers (Nagel et al. 2021, Zieger et al. 2020) and occur mainly at frequencies below 10 Hz. It is reported that the expansion of nearby wind energy installations reduces the quality of gravity wave observations (Saccorotti et al. 2011) or seismological recordings at many sites (Neuffer and Kremers 2017, Pilger and Ceranna 2017, Stammler and Ceranna 2016, Zieger and Ritter 2018). As a consequence, (micro-) earthquake detection capabilities are reduced for state earthquake services when more and more recording sites are surrounded by an increasing number of WTs. So far, two possibilities to suppress WT emissions have been discussed. One is the suppression of emissions by structural measures which has been analyzed with synthetic wave field simulations by Abreu et al. (2022). Another method is the suppression of WT emissions and other noise signals through AI algorithms which has been successfully applied by Heuel and Friederich (2022). Nevertheless, an influence of the processing on seismic wave amplitudes has been observed which limits earthquake magnitude estimation.

Another measure is to define protection radii around seismological stations (e.g., Lerbs et al. 2020) but this has not been established in a compulsory or unified way yet. For this purpose, a detailed study of WT emissions and the most important factors influencing their radia-

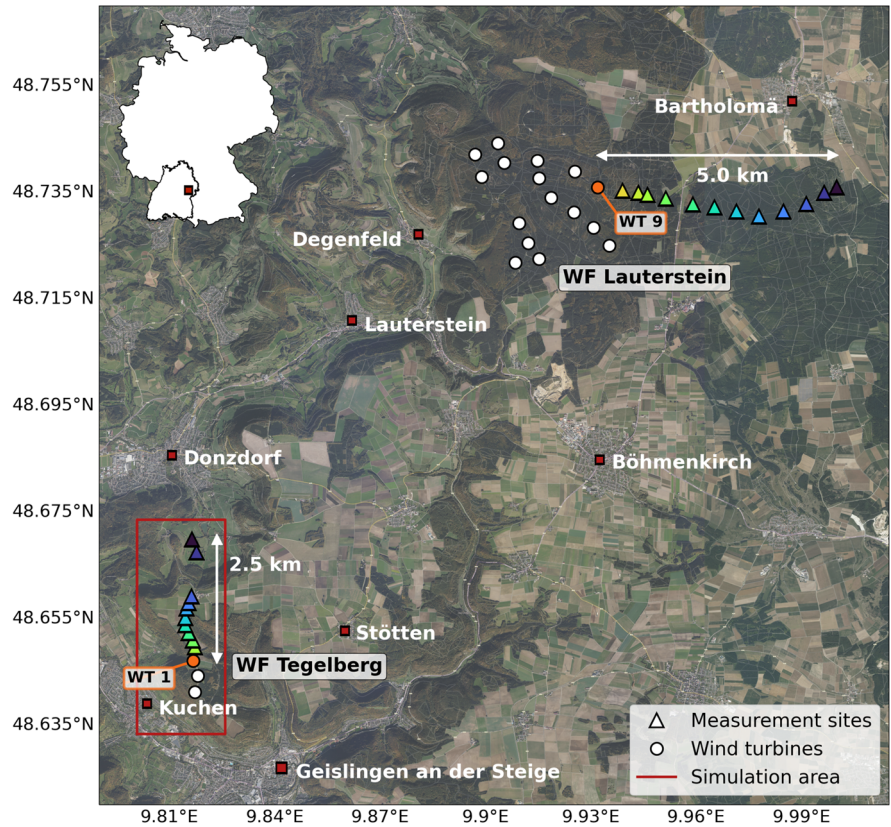
tion is necessary to be able to give recommendations. In the context of the Inter-Wind research project, we conduct measurements that we then use as reference for numerical wave field simulations. Measurements are conducted in the vicinity of two wind farms that lie on a plateau of the Swabian Alb in southwest Germany, near a steep escarpment, the so called Alb cuesta. At the bottom of the escarpment there is the location of settlements, where ground motion measurements had been conducted in two previous campaigns (Gaßner and Ritter 2023a).

Amplitude decay behaviour is related to the subsurface properties, which in our case are layered Jurassic deposits. The subsurface structure combined with the topography and the wind farm geometry are major influences on the wave field propagation. The influence of multiple sources (Limberger et al. 2021) and topography (Limberger et al. 2022) have already been analyzed in previous studies, but still few simulation case studies for WT emissions are available, despite the need to better understand this phenomenon to protect sensitive infrastructure. In our work we use a finite difference (FD) approach to simulate ground motions and focus on directional dependencies, attenuation (Q) and source characteristics. It has been proposed by Neuffer et al. (2021) that different types of surface waves (Rayleigh and Love waves) are radiated by WTs, depending on eigenmode frequency and wind direction. We observe further indications for this behaviour in our data and incorporate an alternative tilt source mechanism in our simulations to reproduce a direction dependent radiation pattern.

2 Measurements and data evaluation

In winter 2021/2022 we conducted two measurement campaigns to record ground motions at two wind farms (Tegelberg and Lauterstein) on the Eastern Swabian Alb (Fig. 1). The main goal was the quantification of the amplitude decay of WT eigenmode signals. For this purpose, 20 instruments were borrowed from the Geophysical Instrument Pool Potsdam (GIPP) at the German Research Center for Geosciences (GFZ). Details on the instrumentation and technical information can be found in Gaßner and Ritter (2023b). Beside the ground motion amplitude decay estimation, recorded data was also analysed for determining seismic phase velocities of the emitted surface waves along the measurement

Fig. 1 Inter-Wind study area with relevant places and locations of WTs (circles). Colored triangles show the recording station positions for measurement campaigns at wind farms (WF) Tegelberg and Lauterstein. Orange circles indicate the WTs where measurements were conducted inside the tower, which are WT 1 at WF Tegelberg and WT 9 at WF Lauterstein. The red box indicates the area for wave field simulation (see Section 3). Inset: Outlines of Germany and the state of Baden-Württemberg. The red marker denotes the location of the study area

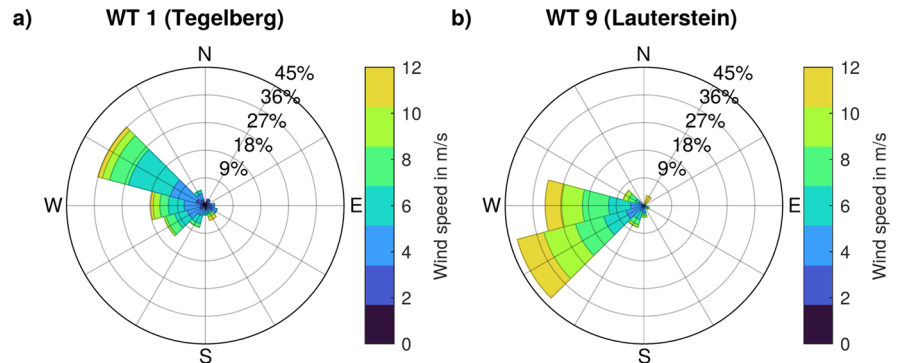


profiles. For data evaluation, WT operating data, such as rotation rate, wind speed and wind direction, was provided by the respective wind farm operators. During both measurement campaigns, the prevailing wind direction was west (Fig. 2), with approximately 40 % of the time wind from WNW at wind farm Tegelberg and WSW at wind farm Lauterstein.

Measurements at wind farm Tegelberg took place from 2021/11/19 to 2021/12/17 and included eight

instruments in a ring-shaped network layout around the northernmost WT (WT 1), one instrument inside WT 1, and ten instruments along a line up to 2.5 km to the north of WT 1 (Fig. 1). The two instruments at the northern end of the line were installed on farm land at lower heights (approximately 510 m height) compared to the other instruments (on average 670 m height). These two, as well as the third-most distant instrument, which was installed in the back yard of a private

Fig. 2 Wind roses displaying the wind speed and wind direction distribution during the measurement campaigns as captured by the respective sensors at the WT where the measurement lines originated. a) at WT 1 of wind farm Tegelberg, b) at WT 9 of wind farm Lauterstein



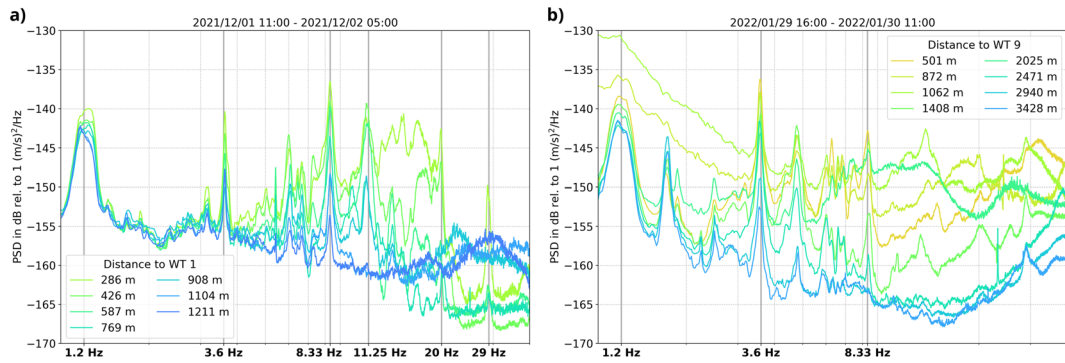


Fig. 3 (updated) Comparison of distance-dependent power spectral densities (PSD) from vertical component data of the line measurements at a) wind farm Tegelberg and b) wind farm

Lauterstein. WT operation related peaks are visible at 1.2 Hz, 3.6 Hz, and 8.33 Hz. Peaks at 11.25 Hz, 20 Hz, and 29 Hz are visible in data from wind farm Tegelberg only

property, were excluded from further data evaluation due to high noise levels. Thus the effective length of the measurement line is 1.2 km (Fig. 3).

At wind farm Lauterstein one instrument was installed on the foundation of one of the easternmost WTs (WT 9), and twelve instruments were installed up to 5 km to the east of WT 9. There, measurements lasted from 2022/01/14 to 2022/02/22. Due to increased noise levels at the instrument sites at the end of the line, only data from eight of the twelve instruments can be used for amplitude decay estimation, limiting the effective line length to 3.4 km for this evaluation (Fig. 3). For phase velocity estimation, data from all instruments was used, because we do not expect the influence of noise to be as critical as for amplitude decay estimation.

Figure 3 shows vertical component data examples from both wind farms. In a distance up to approximately 2.5 km the measurements show three prominent frequency peaks at 1.2 Hz, 3.6 Hz and 8.33 Hz.

Similar frequencies have been observed in other studies (a compilation is shown in Gaßner and Ritter 2023a). Furthermore, we observe three higher-frequency peaks at wind farm Tegelberg only: a peak at 11.25 Hz is detected up to 908 m distance, and peaks at 20 Hz and 29 Hz up to 769 m distance (Fig. 3). The 20 Hz and 29 Hz peaks are not related to the eigenmodes of the WTs but are rotation rate dependent and only occur at full WT operation.

2.1 Phase velocity estimation

Measurements along, more or less, straight profiles allow us to gain insight into the subsurface properties. The propagation of surface waves, induced by the movement of the WT’s foundation provides the opportunity to estimate phase velocities for the observed eigenmode frequencies. The estimated seismic velocities can then be used to characterize the subsurface and

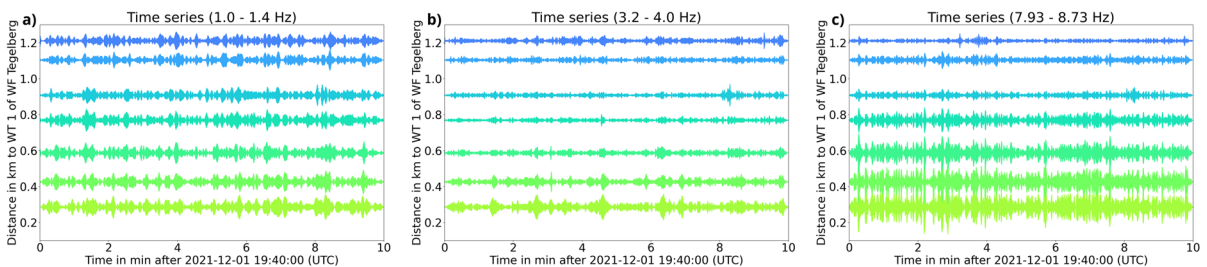


Fig. 4 Signals along the Tegelberg profile for the three frequency ranges used in the phase velocity estimation, indicating the similarity of wave form envelopes between neighbouring stations. a) 1–1.4 Hz, b) 3.2–4 Hz, and c) 7.93–8.73 Hz

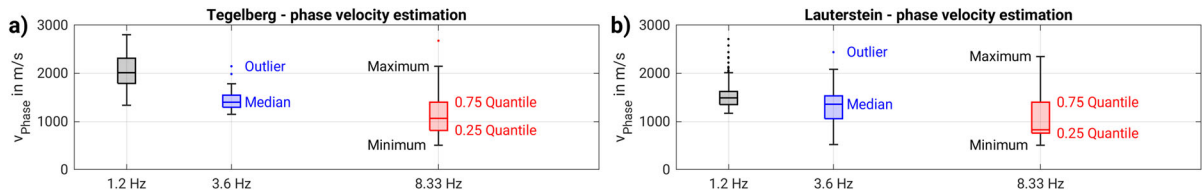


Fig. 5 Seismic phase velocities estimated from recordings at wind farms a) Tegelberg (2021/11/19 to 2021/12/17) and b) Lauterstein (2022/01/14 to 2022/02/22) for frequencies of 1.2 Hz, 3.6 Hz, and 8.33 Hz

to provide seismic velocity information for wave field simulation.

Phase velocities are estimated between every neighboring instrument along the measurement lines, excluding the ring measurement and the three furthest stations at wind farm Tegelberg, and the recordings from within the WT towers at both wind farms. A cross correlation of vertical component 10-minute signals is performed to estimate time shifts related to wave propagation, using the frequency ranges 1–1.4 Hz, 3.2–4 Hz, and 7.93–8.73 Hz, centered around the observed eigenmode frequencies. Data examples for each frequency range from the Tegelberg profile are shown in Fig. 4. Signals are fairly similar along the profiles when the WTs are in operation and external noise sources are expected to be not relevant during the majority of the time windows for both wind farms and measurement periods. During the respective campaigns, at approximately 28.4 % of the evaluated time, none of the three WTs was running at wind farm Tegelberg (rotation rate of all WTs <0.5 rpm). The northernmost WT, WT 1, was running at 63.1 % of the considered time interval (rotation rate >0.5 rpm). At wind farm Lauterstein only at 2.2 % of the time, none of the WTs was in operation. All 10-minute time windows in a selected time frame are evaluated to gain a broad data range. For wind farm Tegelberg, time windows from 2021/11/27 to 2021/12/16 (20 days – 2880 time windows) are considered, and for wind farm Lauterstein data from 2022/01/29 to 2022/02/21 (24 days – 3456 time windows).

From the calculated time shifts, seismic phase velocities are estimated by using the relative distance of the stations to the reference WT (WT 1 at wind farm Tegelberg and WT 9 at wind farm Lauterstein). Every velocity estimate ranging between 500 m/s and 3000 m/s is taken into account for statistical evaluation (Fig. 5) and is counted as a successful estimate in the following. The median value for each frequency range is then

taken as the final result (Table 1). From velocities v and frequencies f , wavelengths can be estimated with $\lambda = v/f$. These depth estimates are then used to construct a velocity–depth model (see Section 3). Higher frequencies have a lower penetration depth than waves with lower frequencies. Seismic velocities typically increase with depth, due to an increase in compaction related to the weight of the overburden. It has to be noted that the estimated velocity values are a mean value representing the whole penetration depth range.

Estimated median surface wave velocities range between 830 m/s and 2010 m/s, with lowest values at 8.33 Hz and highest values at 1.2 Hz (Table 1). The calculated velocities span a relatively large range (difference between box plot minimum and maximum, ~ 1800 m/s, Fig. 5), with the lowest span (~ 600 m/s) found at 3.6 Hz in data from wind farm Tegelberg and ~ 800 m/s at 1.2 Hz for data from wind farm Lauterstein. Within these ranges, velocities are similar for each frequency for data from both wind farms. The highest discrepancy is found at 1.2 Hz, for which the velocity determined at wind farm Tegelberg is one third higher than the one determined at wind farm Lauterstein (~ 2000 m/s compared to ~ 1500 m/s). Velocities of ~ 1400 m/s at 3.6 Hz are the most similar at the two wind farms. Resulting wavelengths from the estimated velocities range between approximately 100 m for 8.33 Hz to approximately 1.5 km for 1.2 Hz (Table 1).

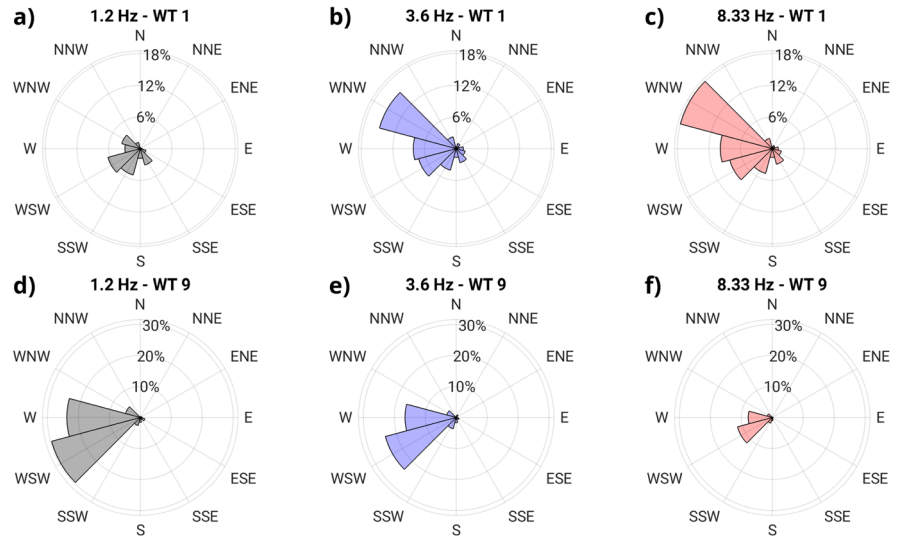
The percentage of successful estimates (within 500 m/s to 3000 m/s) for each time window and station pair (Table 1) increases with frequency at wind farm Tegelberg and decreases in success with frequency for wind farm Lauterstein. The layout of the measurements at wind farm Tegelberg with a profile length (1.3 km) less than the estimated wavelength for 1.2 Hz (1.7 km) is likely a reason for this observation. At wind farm Lauterstein the profile is about four times as long as at wind farm Tegelberg, therefore, signals at 8.33 Hz are

Table 1 Estimated seismic phase velocities for wind farms Tegelberg and Lauterstein with the respective wave lengths and estimation success in the analyzed time interval (relative number of estimates within the velocity range of 500–3000 m/s)

Frequency	Median velocity in m/s (min - max)		Wave length in m		Estimation success in %	
	Tegelberg	Lauterstein	Tegelberg	Lauterstein	Tegelberg	Lauterstein
1.2 Hz	2010 (1340 - 2800)	1490 (1170 - 2010)	1675	1240	26.2	66.2
3.6 Hz	1400 (1150 - 1780)	1360 (520 - 2080)	390	380	46.4	51.7
8.33 Hz	1070 (510 - 2140)	830 (510 - 2350)	130	100	52.0	25.1

At wind farm Tegelberg 2880 and at wind farm Lauterstein 3456 10-min time windows are considered

Fig. 6 Phase velocity estimation success in percent depending on wind direction for each frequency a)+d) 1.2 Hz, b)+e) 3.6 Hz, and c)+f) 8.33 Hz) at a)-c) WT 1 of wind farm Tegelberg and d)-f) at WT 9 of wind farm Lauterstein



already reduced in amplitude and, hence, the correlation is lower (Fig. 4).

Furthermore, a dependency of successful estimates on wind direction can be observed at wind farm Tegelberg (Fig. 6), with most successful estimates at 3.6 Hz and 8.33 Hz for time windows associated with a main wind direction from WNW. For 1.2 Hz more successful estimates are found for wind directions WSW and SSW compared to time windows with wind from WNW. This observation could indicate that waves emitted at 1.2 Hz are only prominent enough during the time windows with a wind direction perpendicular to the main wind direction. For 3.6 Hz and 8.33 Hz this does not seem to be the case. For wind farm Lauterstein no such effect can be observed and for each frequency a similar wind direction distribution of successful estimates is found.

2.2 Amplitude decay estimation

To define protection radii for seismological or other sensitive instruments, the amplitude decay behaviour of WT emissions has to be studied for different geological settings. To predict ground motion amplitudes A in a specific distance r , the factors influencing the amplitude decay have to be known. Studies indicate that the simple relationship, $A \sim 1/r^{b_{amp}}$, where b incorporates effects like geometrical spreading, sub-surface intrinsic attenuation, and scattering, is a valid approach to describe amplitude decay (e.g., Zieger and Ritter, 2018; Neuffer et al. 2019; Lerbs et al. 2020).

Typically, power spectral densities (PSD) are used to estimate b_{PSD} -values, whereas rms-amplitudes as input result in

$$b_{amp} = 0.5 \cdot b_{PSD}. \tag{1}$$

A value of $b_{amp} = 0.5$ ($b_{PSD} = 1$) is the theoretical value for geometrical spreading of surface waves in the far-field in elastic, laterally homogeneous media. Nevertheless, b_{PSD} -values < 1 are found in several studies (Limberger et al. 2021, Neuffer et al. 2019, 2021, Zieger and Ritter 2018) especially for low frequencies (< 5 Hz). The reason for this may be the interference of the wavefields of several WTs. b_{PSD} -values > 1 are related to anelastic damping and increased scattering at smaller wavelengths (~ 100 m) and, therefore, expected for higher frequencies.

As suggested by Gaßner and Ritter (2023a) we compare results using PSD values of eigenmode frequency peaks and ΔPSD values, correcting PSD peak values by values determined for the same frequency in a time window with no WT operation. Thereby, we reduce the effect of other constantly active noise sources. This can be beneficial for sites with nearby industrial compounds or traffic routes which generate a background noise level independent of the distance to the WTs but dependent on the distance to the noise source. Close to our recording sites there are no heavily used traffic routes or similar noise sources though.

We compare b -values estimated for different numbers of WTs running in separate time windows for wind

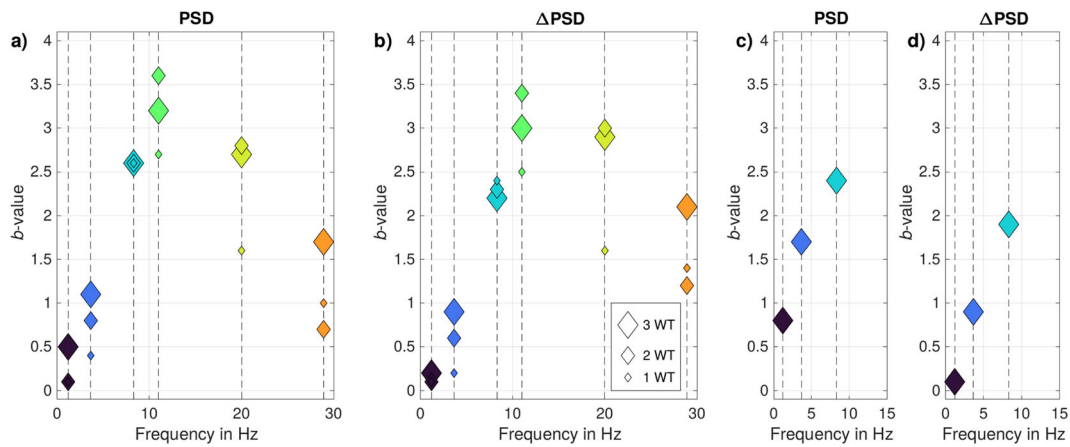


Fig. 7 b_{PSD} -values estimated for selected time windows from measurements at a)–b) wind farm Tegelberg and c)–d) wind farm Lauterstein. For the estimation a)+c) PSD and b)+d) relative PSD

values were used. Colors correspond to the respective analyzed frequency and size to the number of WTs in operation (wind farm Tegelberg)

farm Tegelberg (Fig. 7a and b). Time windows of similar operating conditions are averaged and weighted by their respective duration. We compare time windows when all three, two, or only one WT were in operation (Fig. 7a and b, decreasing symbol size). A reference time window with no WT operation was selected, which lasted 56 h and occurred at the beginning of the measurement campaign. Three time windows are selected when all 3 WTs were in operation with a duration of 10 h to 20 h. Time windows with a single or two WTs in operation occurred with two different WT configurations each for approximately 5 h, respectively.

At wind farm Lauterstein there was a period of 18 h with no WT operation which we use for reference. Six time windows of 10 h to 20 h are chosen with 9 WTs to 15 WTs in operation and a westerly wind direction. They all represent full WT operation, because we do not observe any differences in the PSD amplitudes between these numbers of WTs in operation.

Resulting b -values (Table 2) range from $b_{\text{PSD}} \sim 0.5$ to $b_{\text{PSD}} \sim 3$ for the eigenmode frequencies of the WTs (1.2 Hz – 11.25 Hz) and they increase almost linearly with frequency (Fig. 7, large symbols). For higher frequencies (>20 Hz) b -values are lower than for the maximum eigenmode frequency at 11.25 Hz at wind farm Tegelberg. The high frequencies are related to the WTs generator and gears at full operation (20 Hz and 29 Hz). Discrepancies in b -values for a different number of WTs in operation are lowest for 8.33 Hz and largest for 20 Hz (Fig. 7a and b, symbol size). Overall the results agree well for both wind farms and the two approaches, using PSD and Δ PSD values.

At 3.6 Hz a b -value of $b_{\text{PSD}} \sim 1$ (Table 2) is found for data from both wind farms and methods, matching the theoretical amplitude decay for geometrical spreading of surface waves. The only exception is the result for wind farm Lauterstein using PSD values with $b_{\text{PSD}} = 1.7$. In the following, we use 3.6 Hz as the main

Table 2 Amplitude decay b_{PSD} -values and comparison of the use of PSD and relative PSD values, for full operation periods at wind farms Tegelberg (1.2 Hz to 29 Hz) and Lauterstein (1.2 Hz to 8.33 Hz)

	1.2 Hz	3.6 Hz	8.33 Hz	11.25 Hz	20 Hz	29 Hz
Tegelberg (PSD)	0.5	1.1	2.6	3.2	2.7	1.7
Tegelberg (Δ PSD)	0.2	0.9	2.2	3.0	2.9	2.1
Lauterstein (PSD)	0.8	1.7	2.4	-	-	-
Lauterstein (Δ PSD)	0.1	0.9	1.9	-	-	-

frequency for wave field simulation and $b_{\text{amp}} = 0.5$ ($b_{\text{PSD}} = 1$) as a reference value, because it represents surface wave propagation without significant near-field effects.

3 Wave field simulation

WTs act as continuous ground motion sources, constantly inducing vibrations into the ground through their foundations. The amplitude of the induced ground motions depends on the wind speed and related rotation rate of the WTs. Other factors are the mass and geometry of the WTs and the coupling of the foundation to the ground. Excited frequencies are constant (<12 Hz) or a multiple of the blade passing frequency (BPF). Here, we exemplary study signals at 3.6 Hz which is one of the main eigenmode frequencies excited for the WT type (GE 2.75-120) at wind farm Tegelberg. These WTs have a maximum power production of 2.78 MW and a height of 139 m, with 120 m rotor diameter.

To evaluate the most relevant influences on the wave propagation, we run simulations for a set of different input parameters (Table 3), including three subsurface models, source types (vertical force vs. tilt source) and different source signals (using one WT location as a single source point). Finally, we analyze the effect of topography and the influence of multiple sources (up to 3 WTs) for the geometry of wind farm Tegelberg (Fig. 8). We use a FD approach with a uniform spatial grid (Bohlen 2002).

We simulate wave propagation for 5 s to 15 s, such that the rms-amplitudes can be calculated for approximately 10 cycles from a point in time when the wave field has propagated to all receivers. Thereby, the amplitude decay can be estimated as if a continuous source excitation had been in place. The temporal sampling is set to 0.5 ms to satisfy FD stability criteria.

With the main motivation of this study being the analysis of amplitude decay, we define three different synthetic profiles (Fig. 8). Two of them, the profiles towards the north and south-west, are oriented along the receiver locations chosen during the actual measurement campaigns presented in Fig. 1 and Gaßner and Ritter (2023a). Furthermore, an additional synthetic profile towards the west of WT 1 allows to further study directional dependencies (green line in Fig. 8).

3.1 Model setup

To include all field measurement locations from the campaigns at wind farm Tegelberg, the extent of the model is chosen to be 1.8 km in east-west direction and 4.5 km in north-south direction (Table 4). For the study of attenuation a north-south extension of 27 km is used. The vertical extent of the model is 700 m for simulations with no or single-fold topography. These simulations have a grid spacing of $dh = 10$ m. To study the influence of topography, such as the Alb cuesta, simulations with two-fold topography are calculated. They have a vertical extent of 2.2 km with $dh = 5$ m. An air layer of 15 grid points is used in all simulations to incorporate the boundary condition layer. All subsurface models have a 1-D layered or homogeneous structure, but the geometry and topography is fully 3-D.

3.1.1 Geological model and homogeneous geological model

The Swabian Alb, where the measurement campaigns took place, represents a stratified subsurface of Jurassic layers consisting of limestone, marl, shale, sandstone, and slate (Fig. 9a, LGRB (2021a)). Therefore, we construct a model of the elastic parameters (v_p , v_s , and ρ) based on the geology of the Swabian Alb and petrophysical data (Fig. 9b and Table 5). We extract information on the geology of the layers exposed at the surface of the model area (Fig. 1) from geological maps provided by LGRB (2021b). The geology of the subsurface up to a depth of 490 m was gathered from LGRB (2021a). Consecutive lithologic units of the same rock type were combined to one single layer. At greater depth we assumed a half-space with elastic properties of sandstone, representing Upper Triassic (Keuper), the uppermost lithostatigraphic group of the German Triassic (LGRB 2020). The elastic rock parameters are extracted from Landolt-Börnstein (1982) and Gebrande (1982). To account for the seismic velocity increase with depth we used the simple relation from Tiab and Donaldson (2016)

$$p(z) = 22.7 \text{ kPa} \cdot z, \quad (2)$$

with $p(z)$ the lithostatic pressure-depth relation,

$$v_{p,i}(z) = v_{p,i} + p(z) \cdot \gamma \quad (3)$$

Table 3 Overview of all simulations. PVE - phase velocity estimation model, G - geological model, HG - homogeneous geological model

Figure	Model	Topography	$Q/P/S$	Source type	Source time function	Sources	ID
10	PVE	-	-	vertical	sine (3.6 Hz)	1	A
	G	-	-	vertical	sine (3.6 Hz)	1	B
	HG	-	-	vertical	sine (3.6 Hz)	1	C
11	HG	-	-	vertical	sine (3.6 Hz)	1	D
	HG	-	50	vertical	sine (3.6 Hz)	1	
	HG	-	100	vertical	sine (3.6 Hz)	1	
	HG	-	200	vertical	sine (3.6 Hz)	1	
14a	PVE	-	-	vertical	sine (3.6 Hz)	1	G
	PVE	-	-	tilt (N-S)	sine (3.6 Hz)	1	
	PVE	-	-	tilt (E-W)	sine (3.6 Hz)	1	
14b	PVE	-	-	vertical	1 - sine (3.6 Hz)	1	I
	PVE	-	-	vertical	2 - sine (1.2; Hz 3.6; Hz 8.33 Hz)	1	
	PVE	-	-	vertical	3 - real (3.2 Hz - 4.0 Hz)	1	
	PVE	-	-	vertical	4 - real (1.0 Hz - 9.0 Hz)	1	
14c	PVE	-	-	vertical	sine (3.6 Hz)	3	L
	PVE	-	-	vertical	sine (1.2; Hz 3.6; Hz 8.33 Hz)	3	
15a	HG	-	-	vertical	sine (3.6 Hz)	1	N
	HG	1x	-	vertical	sine (3.6 Hz)	1	
	HG	2x	-	vertical	sine (3.6 Hz)	1	
15b	PVE	-	-	vertical	sine (3.6 Hz)	1	P
	PVE	-	-	vertical	sine (3.6 Hz)	3	
	PVE	1x	-	vertical	sine (3.6 Hz)	3	

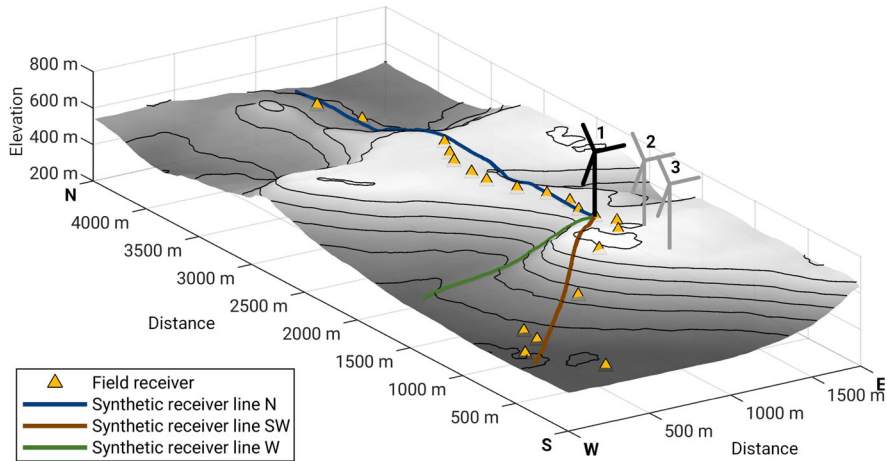


Fig. 8 Overview of the model area and its topography (interpolated from SRTM 1 s data) used for the emission simulation at wind farm Tegelberg. The locations of the sources (WTs) are displayed, as well as the synthetic receivers corresponding to the

field instrument positions (marked as triangles) and the virtual receivers at each grid point along three synthetic profiles starting at WT 1 (north - blue, south west - red, west - green). The origin of the model area is situated at 9.8008°E and 48.6333°N

$v_{p,i}$ P-wave velocity of the i -th layer, and the velocity-pressure ratio $\gamma = 3 \cdot 10^{-5}$ (mean value of Mayr and Burkhardt 2005; Barton 2007). Furthermore, we compose a homogeneous geological model representing a half-space. Its elastic parameters are calculated using the weighted mean of the elastic parameters of the geological model (Fig. 9c and Table 5).

3.1.2 Phase velocity estimation model

The results from phase velocity estimation at wind farm Tegelberg (Section 2.1) are used to construct a three-layer S-wave velocity model (Fig. 9). Depth interfaces between the individual layers are adopted from the geological model, matching the approximate penetration depth estimated from the analyzed wave lengths (Table 1). The P-wave velocity model is calculated with

the relation $v_p = v_s \cdot \sqrt{3}$, and the density model was adopted from the homogeneous geological model. This model is referred to as PVE model in the following.

3.2 Effect of the subsurface

The amplitude decay determined from simulations with the three different subsurface models are compared in this subsection, as well as the effect of attenuation within the homogeneous subsurface model. A single source with vertical force excitation and a 3.6 Hz sine signal are used, and no topography is considered (Table 3, simulations A-C). For wave field simulation, the northernmost of the ring stations was used as reference, at approximately 150 m distance to WT 1 to be consistent with measurement results shown in Gaßner

Table 4 Model setup for different simulations

Study	Model dimensions in m			dh in m
	E	N	Z	
Regular	1800	4500	700	10
Attenuation	1800	27000	700	10
Topography	1800	4500	700/2200	5

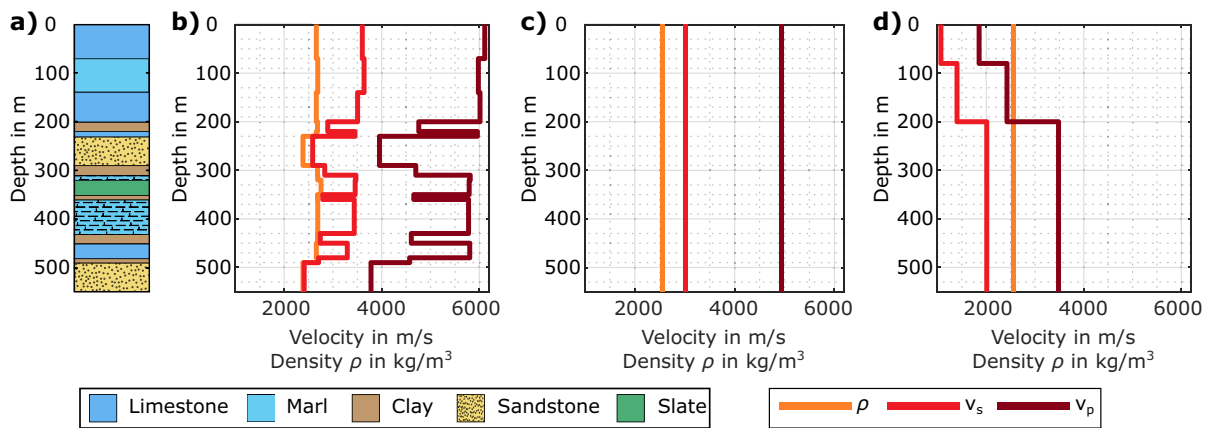


Fig. 9 (updated) Subsurface parameter distributions. a) stratigraphy adapted from LGRB (2020, 2021a), elastic parameters for b) the geological model (G), c) the homogeneous geological model (HG), and d) the phase velocity estimation model (PVE)

and Ritter (2023a) where the nearest station was also installed in 150 m distance to WT 1.

3.2.1 Model comparison

The seismic velocities derived from geological information (maps and average elastic parameters, LGRB 2021b; Landolt-Börnstein 1982; Gebrande 1982) and phase velocity estimation from measurements (Section 2.1) differ significantly, with much lower velocities found by the analysis of real waveform data compared to parameters from literature (Fig. 9). The use of such different models provides the opportunity to compare the effect of uncertainties in parameter estimation.

Resulting amplitude decay curves exhibit a stronger amplitude decay ($b_{amp} \sim 0.8$) for the geological model than for the homogeneous geological model, and a stronger undulation of the decay curve for the PVE

Table 5 Elastic parameters (v_p – P-wave velocity, v_s – S-wave velocity, ρ – density) for the geological and homogeneous geological models

Geological unit	Elastic parameters		
	v_p in m/s	v_s in m/s	ρ in kg/m^3
Limestone	5630	3120	2658
Marl	5545	3201	2688
Shale	4415	2549	2683
Sandstone	3630	2260	2385
Slate	5530	3193	2755
Weighted mean	4946	3007	2563

model which fits a b -value of $b_{amp} \sim 0.5$ (Fig. 10), consistent with findings in Section 2.2.

3.2.2 Attenuation

To study the influence of subsurface intrinsic attenuation (represented by the quality factor Q) on the amplitude decay, we use the homogeneous geological model without topography and a single, vertical source, with sine excitation. The effect of attenuation on the waveform increases with distance. Therefore, we enlarge our model in the northern direction to be able to simulate a wave field propagation along a profile of up to a distance of 30 wavelengths (compare Table 4).

We use constant Q values of 50, 100, and 200 and compare the amplitude decay along the extended north

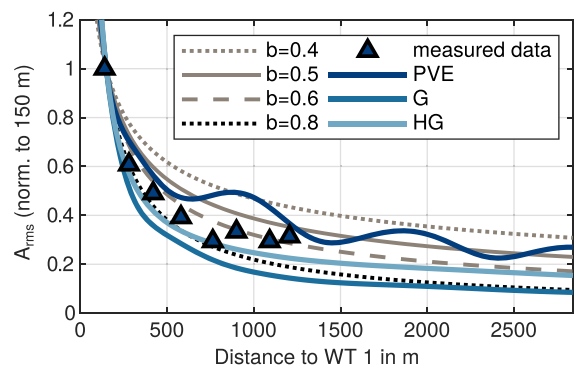


Fig. 10 Amplitude decay curves along the north profile showing the influence of the different subsurface models. For these simulations no topography and one source with vertical excitation was used

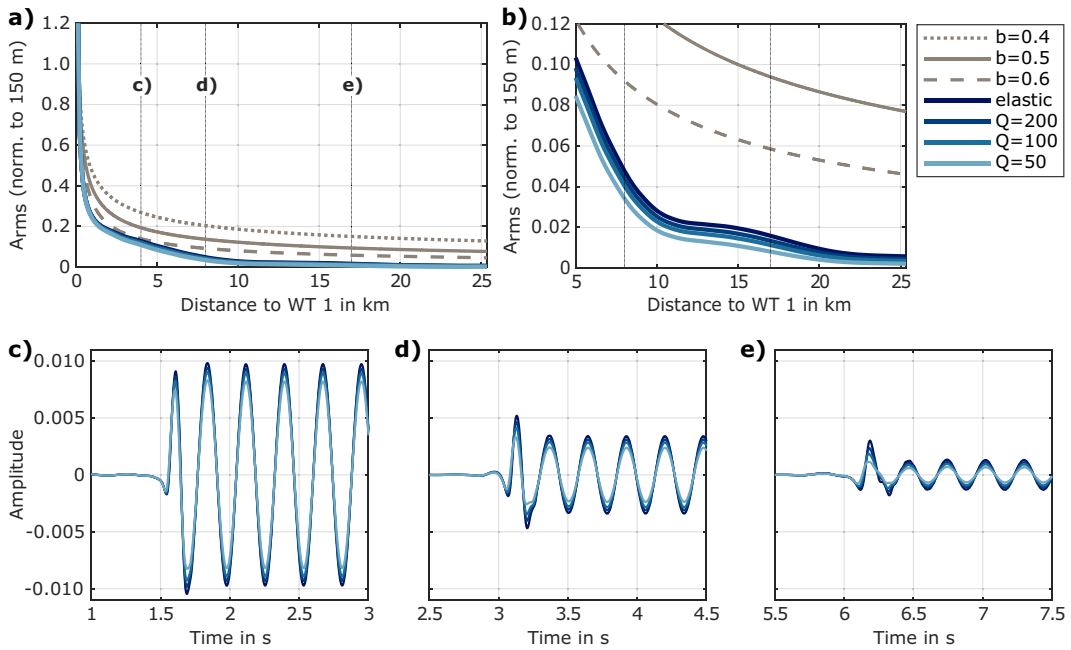


Fig. 11 a) Amplitude decay curves along an extended north profile showing the influence of Q . b) Zoom at distances larger than 5 km. For these simulations no topography and a source with

vertical excitation was used. Seismograms at c) 5λ , d) 10λ and e) 20λ (4 km, 8 km, and 17 km distance to WT 1), showing the effect of attenuation as well as geometrical spreading

profile. These Q values, chosen from Barton (2007) and Schön (1996), are representative for the actual present geology. The effect of different attenuation models is very limited on the amplitude decay as well as on the respective wave forms (Fig. 11). The shown

seismograms at distances of 4 km to 17 km correspond to a propagation distance of 5 to 20 wavelengths. At these distances no prominent effects due to intrinsic damping (Q) can be observed. The main influence on waveform amplitudes is clearly geometrical spreading.

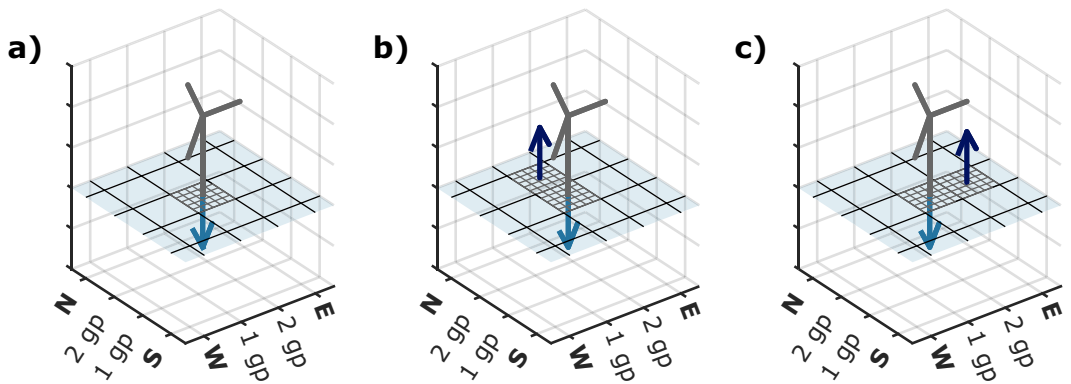


Fig. 12 Sketch showing the different source types. a) vertical source, b) tilt source with orientation towards north, c) tilt source with orientation towards east. Tilt sources are realized by an addi-

tional force source at a neighbouring grid point (gp) excited with an inversely polarized source signal

3.3 Effect of source configuration

WT sources are implemented in a FD approach in a simplified way as a vertical force, fed by a continuous source signal. Here, we compare the effect of source implementation and different source time functions (synthetic and derived from measurements) on the emitted ground motions.

3.3.1 Source type

A vertical force source at the WT location is implemented by adding a source signal to the vertical ground motion velocity component. It can be conceived as an approximation of an up-and-down moving object inducing a force at the Earth's surface. More realistically is a tilt of the WT foundation which is implemented by using two adjacent force sources. Figure 12 shows a sketch of the different source excitation types. We simulate tilting towards north and towards east by adding an additional vertical force source shifted by a grid point towards the respective direction. The source signal at the second source point is inversely polarized compared to the signal at the first source point. The grid point spacing of $dh = 10$ m corresponds well with the actual diameter of the WT foundation, which is approximately 10.5 m.

3.3.2 Source time function

As a standard source time function we use a tapered sine signal with 3.6 Hz (signal 1, Fig. 13a). Additionally, we construct a synthetic signal (signal 2, Fig. 13b) with the combination of three differently phase-shifted sines at 1.2 Hz (phase shift $\Phi = 0.25\pi$), 3.6 Hz ($\Phi = 0.5\pi$), and 8.33 Hz ($\Phi = 0.75\pi$) representing three of the observed WT eigenmode frequencies. Furthermore, we use two bandpass filtered, measured signals from our recordings on the foundation of WT 1 with corner frequencies of 3.2 Hz and 4.0 Hz (narrow band, signal 3, Fig. 13c), and 1 Hz and 9 Hz (broad band, signal 4, Fig. 13d), respectively. The simulation time is set to 5 s for the narrow band 3.6 Hz sine signal and 15 s for all other signals, due to their higher waveform complexity.

3.3.3 Number of sources

Wind farm Tegelberg consists of three WTs of which we studied the northernmost WT (WT 1) in all previ-

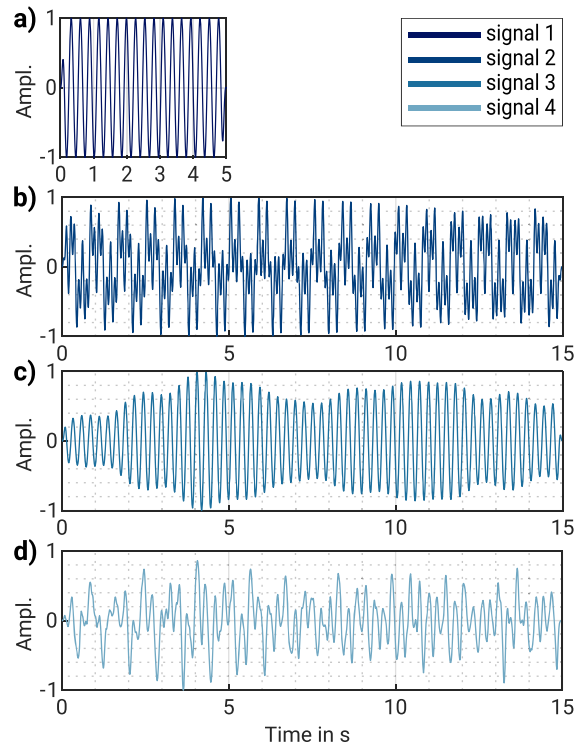


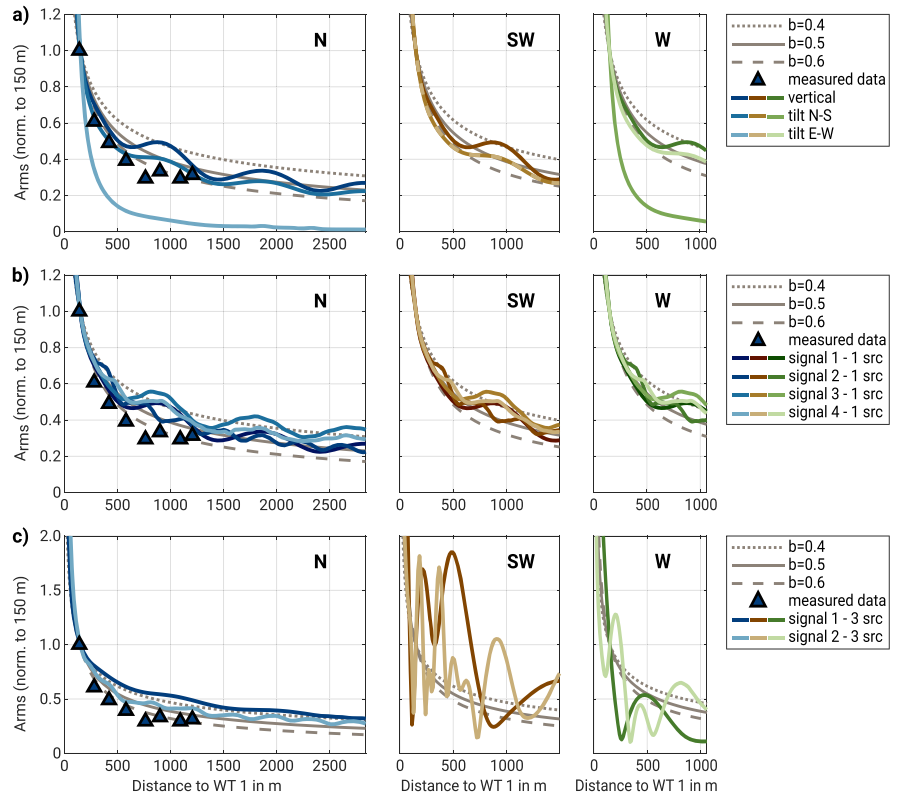
Fig. 13 Source time functions. a) synthetic sine signal at 3.6 Hz (signal 1), b) synthetic sine signals composed of the typical eigenmode frequencies, 1.2 Hz, 3.6 Hz, and 8.33 Hz (signal 2), c) recorded signal filtered between 3.2 Hz and 4.0 Hz (narrow band, signal 3), and d) recorded signal filtered between 1 Hz and 9 Hz (broad band, signal 4)

ous simulations (Fig. 8, Table 3, simulations A-K). In the following, we compare the single WT simulations to simulations with three sources using two different synthetic source signals, signal 1 and signal 2 and the PVE model (Table 3, simulations L-M).

3.3.4 Amplitude decay for different source configurations

Figure 14 gives an overview of the resulting amplitude decays due to the different source configurations (Table 3, simulations G-M). Comparing a vertical force with east-west and north-south tilting, we find that the amplitude decay is mostly affected along on those profiles that are perpendicularly oriented relative to the tilt movement (N-S tilting on the west profile and E-W tilting on the north profile, Fig. 14a). The decay of the tilt motion is significantly stronger ($b_{\text{amp}} \sim 1.6$) due to the destructive interference of the two emitted sig-

Fig. 14 Influence of the a) source type, b) source function, and c) number of sources in combination with two different synthetic source time functions (bottom). A vertical source excitation and the PVE model are used in these simulations. Colors indicate profile orientation (Fig. 8)



nals. Along those profiles in line with or oblique to the tilt motion, the decay is similar in its appearance, but slightly stronger compared to the one with the vertical force source.

The different types of source signals (signals 1-4) result in a fairly similar amplitude decay (Fig. 14b), all undulating around the curve with a theoretical b -value of $b_{amp} = 0.5$. There is, as expected, no effect for the different profile orientations, because we do not include topography and apply a vertical force source in these simulations. Only the appearance of the amplitude decay curves for signal 2, the combination of three sine signals, differs from those of the other three signals. Therefore, we used for the simulation with three sources merely the two different synthetic sine signals (signals 1 and 2). The effect of multiple sources (Fig. 14c), using the geometry of wind farm Tegelberg, results in complicated amplitude decay curves, especially for the south-west profile and to a lesser extent for the west profile. The two source signals produce different amplitude and interference patterns due to their frequency content related to the wavelengths and relative distance between the WTs. The north pro-

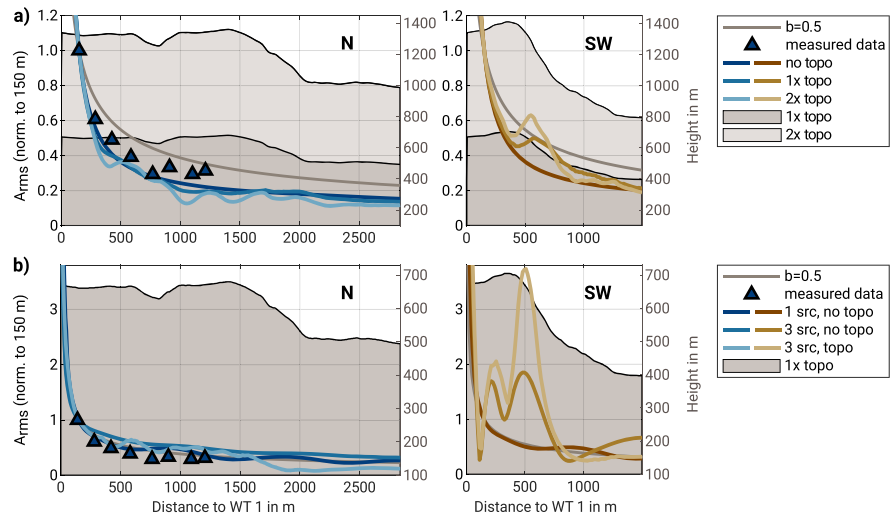
file is not affected and both decay curves show a similar, even smoother decay as for the case of one source due to the north-south oriented layout of the wind farm (Fig. 8).

3.4 Effect of topography

Wind farm Tegelberg is situated on top of the steep escarpment of the Swabian Alb, approximately 300 m above the municipality of Kuchen in 1 km distance towards the southwest. Towards the north of the wind farm, the topography is more flat and forms an elongated plateau (Fig. 8) with a maximum difference in topography of 190 m. Significant topography influences the seismic wave propagation and is considered in simulations, for which the amplitude decay is shown in Fig. 15.

The effect of the actual topography (simulation N) is compared to simulations with no topography and a twofold exaggerated topography (simulation O), expected in other low mountain ranges like the Black Forest, using a homogeneous underground model and a vertical force source (Fig. 15a). Here, stronger

Fig. 15 a) Effect of topography (0×, 1×, and 2× the real topography at wind farm Tegelberg) on the amplitude decay along the N- and SW-profile. A vertical source excitation, a sine signal at 3.6 Hz, and the homogeneous model were used for these simulations. b) Effect of topography in combination with one or multiple sources. A vertical source excitation, a sine signal at 3.6 Hz, and the PVE model were used for these simulations

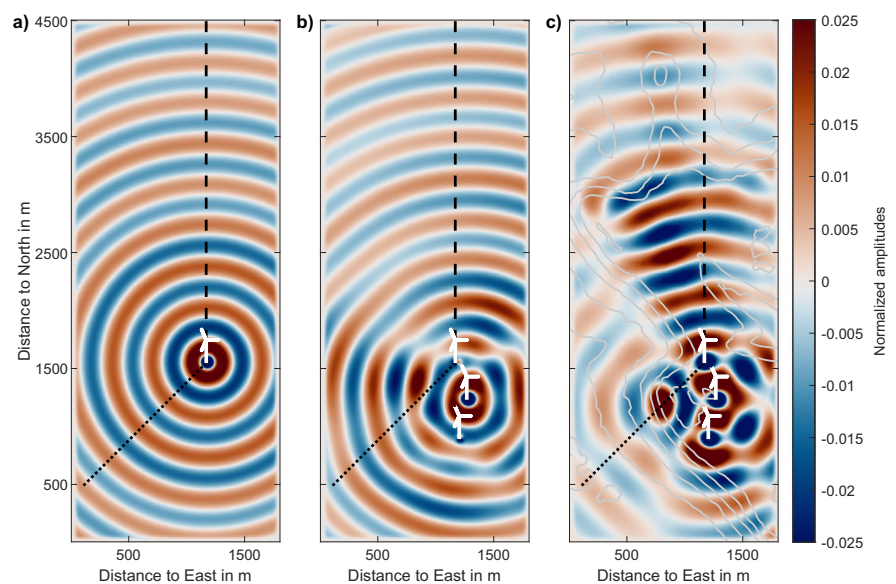


undulations are found in the amplitude decay for higher topography, especially towards the southwest across the simulated steep Alb cuesta.

Figure 15b shows results for a combination of topography with one source and topography without exaggeration, and three sources using the PVE model. This configuration is closest to the actual geometry at wind farm Tegelberg and combines different effects analyzed separately so far. Similar to the amplitude decays shown in Fig. 15a, the decay along the northern profile line only has small variations. In comparison, along the profile

towards the southwest there are strong effects not only due to the topography but also due to the three interfering signals. This combined parameter choice leads to an amplification of the signals by more than three times, mainly caused by the constructive interference of the three sources (Fig. 16). Furthermore, a guiding effect of the topography along the plateau can be observed in Fig. 16c for the simulation including three sources and topography (simulation Q) with increased amplitudes towards north compared to the simulation without topography (Fig. 16b).

Fig. 16 Snapshot of the wave field propagation at 4 s along the model surface for the vertical component. Simulations with a) no topography and one source, b) no topography and three sources, and c) topography and three sources. Contour lines are spaced at 50 m height intervals. Simulations were done with a vertical source excitation, a sine signal at 3.6 Hz, and the PVE model. Black dashed lines indicate the north profile and dotted lines the south west profile



4 Discussion

The quantification and prediction of WT emissions is related strongly to the knowledge of radiation mechanisms and of the subsurface petrophysical properties in the vicinity of the specific WT sites. In this study we analyze data from two wind farms on plateaus of the Swabian Alb. Both wind farms comprise the same WT type and are erected at comparable sites within a forest. The measurement profiles are installed on farm land and forest sites along similar geological conditions on Upper Jurassic limestone. Therefore, we expect results concerning phase velocity and amplitude decay to be similar.

Our data evaluation shows that this is the case for the estimated surface waves at WT-eigenmode frequencies of 3.6 Hz and 8.33 Hz. At both frequencies the resulting phase velocities are similar, though the velocity range of valid estimations is much wider for 3.6 Hz at wind farm Lauterstein than at wind farm Tegelberg. The opposite is the case for the estimated velocities at 1.2 Hz, where a wider range is observed at wind farm Tegelberg. At 1.2 Hz there is also a larger discrepancy in the estimated phase velocities (Table 1).

These different ranges found at 1.2 Hz and 3.6 Hz could point at the mechanism observed by Neuffer et al. (2021). They propose that different types of surface waves (Rayleigh or Love waves) are radiated in cross or down wind direction depending on WT eigenmode frequency. Our observation is in accordance with the proposed mechanism where Love waves are radiated in cross wind direction for 1.2 Hz (1.1 Hz in Neuffer et al. 2021) and in down wind direction for 3.6 Hz (3.25 Hz in Neuffer et al. 2021). With the main wind direction being west during our surveys (Fig. 2), a profile oriented to the north (like at wind farm Tegelberg) would feature Love waves at 1.2 Hz and a profile towards east (wind farm Lauterstein) at 3.6 Hz. Due to the Love wave polarisation (horizontally, perpendicular to the propagation direction) an analysis of the horizontal component data would, therefore, be reasonable in the future. Our analysis of vertical component data is more suited for Rayleigh waves.

Another possible explanation for the less successful analysis of data at 1.2 Hz could be the fact that the wavelength (~ 1.7 km) is simply too large and the profile at wind farm Tegelberg too short (1.2 km). Even the profile at wind farm Lauterstein with 5 km length only includes three wavelengths at 1.2 Hz. Thus near-

field effects can influence the seismic wave field and distort typical wave type properties such as polarisation and amplitude behaviour. At wind farm Tegelberg there is likely an interaction with the topography, which is highly variable on a kilometer scale (Fig. 8) with topographic differences of approximately 300 m across the Alb cuesta. Therefore, we assume it is reasonable to focus on the analysis of the 3.6 Hz eigenmode in further data evaluation, as we do in the numerical wave field simulation.

In the amplitude decay estimation we find b_{PSD} -values for the eigenmode frequencies of 1.2 Hz, 3.6 Hz and 8.33 Hz which are consistent for both wind farms. This finding supports our assumption that the geological underground is comparable between both sites. There are differences between the wind farm locations in b_{PSD} of up to 0.6 using PSD maxima and of 0.3 using ΔPSD . Differences between both methods (PSD and ΔPSD) are up to 0.8 at wind farm Lauterstein and up to 0.4 at wind farm Tegelberg. This indicates that there might be an additional background noise source near wind farm Lauterstein, potentially influencing the ground motion amplitudes along the profile. Overall, we find $b_{\text{PSD}} < 1$ for 1.2 Hz, $b_{\text{PSD}} \sim 1$ at 3.6 Hz and $1.7 < b_{\text{PSD}} < 3.2$ for higher frequencies, which include two rotation rate dependent frequency peaks at wind farm Tegelberg. Compared to Gaßner and Ritter (2023a) estimated b_{PSD} -values are much more consistent due to the orientation of both profiles away from settlements, towards farm land and forest sites. Additionally, we analyze recordings along profiles with less topography, compared to the measurements analyzed by Gaßner and Ritter (2023a).

The simulation of WT emissions, using an FD approach, provides us with the opportunity to study the effect of subsurface properties, topography and source configuration on the amplitude decay of the WT induced ground motions. We built layered subsurface models, with parameters gathered from a) geological data and b) phase velocity estimation. Here we observe strong discrepancies in seismic velocities between the geological model and the PVE model. Geological and petrophysical data indicate high shallow velocities, but estimated phase velocities are lower. This hints at weathering, fissures, or Karst effects along the actual measurement profiles, which would potentially reduce in-situ seismic velocities. Nevertheless, we use the contrasting models to compare the influence of the different subsurface parameters. Addition-

ally, we compare wave propagation in layered media with a homogeneous model. To generate Love waves excited by the WTs, a layered structure with a velocity increase with depth is required. This is only the case for the PVE model in our simulations. Furthermore, a source type is required which can reproduce radiation of different wave types as observed by Neuffer et al. (2021). This is achieved by the tilting source in our simulations. With this approach we can model and reproduce the observed wind direction dependency on the excited wave types.

In our simulation study we focus on wave propagation from one source at first, to analyze the effects of the subsurface and source excitation separately. Next, we include the influence of the wind farm layout and the topography, like it is done in Limberger et al. (2022) but additionally we use a layered subsurface model. Limberger et al. (2021) have shown that the interplay of multiple sources and phase differences play a major role in the amplitude decay analysis. Therefore, the layout and also potential heterogeneity of wind farms with different WT types and eigenmodes requires an individual characterization. Finally, the knowledge about wind directions should be incorporated when estimating amplitude decay for specific sites.

5 Conclusion

In this work we analyze data from two ground motion measurement campaigns at two wind farms situated near the Swabian Alb cuesta. Along the measurement lines we estimate seismic phase velocities ($v \leq 2000$ m/s) for surface waves emitted at the eigenmode frequencies of the WT towers (1.2 Hz to 8.33 Hz) and also determine amplitude decay b -values. Due to the similarities in geology at the WT and measurement sites and the same WT type comprising the two wind farms we obtain comparable results for the seismic phase velocities as well as b -values characterizing the amplitude decay at the two sites. Results are especially consistent for a frequency of 3.6 Hz with $b_{\text{PSD}} \sim 1$ and are, therefore, studied in 3-D FD wave field simulation. The determined surface wave velocities are compared to a petrophysical model built from literature values (Landolt-Börnstein 1982; Gebrande 1982, $v_S \sim 3000$ m/s), which we find differ

significantly from our data analysis. Thus, we analyze the effect of the different subsurface parameters on the wave field propagation by using two different layered models.

Additionally to the subsurface parameters, we study the influence of the source implementation as well as the interplay between multiple sources and topography. Because we observe dependencies on wind direction in our data evaluation, we use a source type reflecting the tilting motion of the WT foundation which introduces directional dependencies in the emitted wave fields. This has a more significant effect on the amplitude decay than the different petrophysical parameters that we compared before. Furthermore, we observe that the main influence on the amplitude decay is geometrical spreading and the effect of subsurface attenuation is negligible for the setup shown in this study. In the future, a combination of directional dependent wave field radiation with different complexities of a wind farm (WT types and layout) should be considered to further improve the prediction of site specific WT emissions.

Acknowledgements We thank two anonymous reviewers for valuable comments and suggestions. The local authorities of the municipalities Kuchen, Donzdorf, and Bartholomä are acknowledged for their support. We also thank the Stadtwerke Schwäbisch Hall and the KWA Contracting AG for providing access to WT 1 and the WT operating data at wind farm Tegelberg, as well as the wpd windmanager technik GmbH for access and data related to wind farm Lauterstein. We acknowledge the support of local residents, Forst BW and the Regierungspräsidium Stuttgart (department 56) that allowed the installation of instruments on their property. Felix Bögelspacher, Leon Merkel, Rune Helk, Ankitha Pezhery, and Amelie Nüsse helped with the installation and maintenance of the ground motion sensors. We thank Thomas Forbriger for helpful comments on the manuscript. Devices for the field measurements were provided by the German Research Centre for Geosciences (GFZ) Geophysical Instrument Pool Potsdam (GIPP). Maps were prepared using Cartopy (Met Office 2010 - 2015).

Author contributions All authors developed the concept of the study. L.G. was responsible for the measurements, the field data analysis and writing of the main manuscript. M.G. performed the numerical simulations and produced the corresponding figures. J.R. supervised the writing of and edited the article.

Funding Information Open Access funding enabled and organized by Projekt DEAL. This study is supported by the Federal Ministry for Economic Affairs and Climate Action based on a resolution of the German Bundestag (grant no. 03EE2023D). We acknowledge support by the KIT-Publication Fund of the Karlsruhe Institute of Technology.

Data Availability Statement Seismological data is published under the network code 4C and available at <http://ws.gpi.kit.edu/fdsnws/>.

Code Availability Code used in this research can be made available upon request. The simulation software used in this study can be downloaded at <https://gitlab.kit.edu/kit/gpi/ag/software/wave/wave-simulation>.

Declarations

Competing interests The authors declare no competing interests.

Open Access This article is licensed under a Creative Commons Attribution 4.0 International License, which permits use, sharing, adaptation, distribution and reproduction in any medium or format, as long as you give appropriate credit to the original author(s) and the source, provide a link to the Creative Commons licence, and indicate if changes were made. The images or other third party material in this article are included in the article's Creative Commons licence, unless indicated otherwise in a credit line to the material. If material is not included in the article's Creative Commons licence and your intended use is not permitted by statutory regulation or exceeds the permitted use, you will need to obtain permission directly from the copyright holder. To view a copy of this licence, visit <http://creativecommons.org/licenses/by/4.0/>.

References

- Abreu R, Peter D, Thomas C (2022) Reduction of wind-turbine-generated seismic noise with structural measures. *Wind Energy Sci* 7(3):1227–1239
- Ascone L, Kling C, Wiczorek J, Koch C, Kühn S (2021) A longitudinal, randomized experimental pilot study to investigate the effects of airborne infrasound on human mental health, cognition, and brain structure. *Sci Rep* 11(1):3190
- Barton N (2007) Rock quality, seismic velocity, attenuation and anisotropy. *Balkema-proceedings and monographs in engineering, water, and earth sciences*. Taylor & Francis, ISBN 9780415394413
- Bohlen T (2002) Parallel 3-D viscoelastic finite difference seismic modelling. *Comput Geosci* 28(8):887–899
- DIN 4150-2:1999-06 (1999) Erschütterungen im Bauwesen - Teil 2: Einwirkungen auf Menschen in Gebäuden. <https://www.beuth.de/de/norm/din-4150-2/12168614>, Accessed on 03-04-2022
- Gaßner L, Blumendeller E, Müller FJY, Wigger M, Rettenmeier A, Cheng PW, Hübner G, Ritter J, Pohl J (2022) Joint analysis of resident complaints, meteorological, acoustic, and ground motion data to establish a robust annoyance evaluation of wind turbine emissions. *Renewable Energy* 188:1072–1093. <https://doi.org/10.1016/j.renene.2022.02.081>
- Gaßner L, Ritter J (2023a) Ground motion emissions due to wind turbines: observations, acoustic coupling, and attenuation relationships. *Solid Earth* 14:785–803. <https://doi.org/10.5194/se-14-785-2023>
- Gaßner L, Ritter J (2023b) Wind turbine emissions: interdisciplinary analysis and mitigation approaches—project Inter-Wind. Description of datasets "Inter-Wind" and "Inter-Wind (recorder log Files)". <https://geofon.gfz-potsdam.de/doi/network/4C/2020>
- Gebrande H (1982) Subvolume B 3.1.2.1 Rocks: datasheet from Landolt-Börnstein - Group V Geophysics vol 1B: "Subvolume B" in SpringerMaterials, Copyright 1982 Springer-Verlag. Berlin Heidelberg. https://doi.org/10.1007/10201909_2
- Haac TR, Kaliski K, Landis M, Hoen B, Rand J, Firestone J, Elliott D, Hübner G, Pohl J (2019) Wind turbine audibility and noise annoyance in a national us survey: individual perception and influencing factors. *J Acoust Soc Am* 146(2):1124–1141
- Heuel J, Friederich W (2022) Suppression of wind turbine noise from seismological data using nonlinear thresholding and denoising autoencoder. *J Seismolog* 26(5):913–934
- Hübner G, Pohl J, Hoen B, Firestone J, Rand J, Elliott D, Haac R (2019) Monitoring annoyance and stress effects of wind turbines on nearby residents: a comparison of US and European samples. *Environ Int* 132:105090. <https://doi.org/10.1016/j.envint.2019.105090>
- Landolt-Börnstein. Numerical data and functional relationships in science and technology - new series. In Angenheister G (ed) *Physical properties of rocks - vol 1 Subvolume b*. Springer Berlin Heidelberg, ISBN 978-3-540-11070-5. <https://doi.org/10.1007/b20009>
- Lerbs N, Zieger T, Ritter J, Korn M (2020) Wind turbine induced seismic signals: the large-scale SMARTIE1 experiment and a concept to define protection radii for recording stations. *Near Surf Geophys* 18(5):467–482
- LGRB (2020) LGRBwissen - Keuper. <https://lgrbwissen.lgrb-bw.de/geologie/schichtenfolge/trias/keuper>
- LGRB (2021a) LGRBwissen - Jura. <https://lgrbwissen.lgrb-bw.de/geologie/schichtenfolge/jura>
- LGRB 2021b LGRB-Kartenviewer - layer GeoLa-GK50: geological units (areas). <https://maps.lgrb-bw.de/>
- Limberger F, Lindenfeld M, Deckert H, Rumpker G (2021) Seismic radiation from wind turbines: observations and analytical modeling of frequency-dependent amplitude decays. *Solid Earth Discussions* pp 1–26
- Limberger F, Rumpker G, Lindenfeld M, Deckert H (2022) Development of a numerical modelling method to predict the seismic signals generated by wind farms. *Sci Rep* 12(1):15516
- Marshall NS, Cho G, Toelle BG, Tonin R, Bartlett DJ, D'Rozario AL, Evans CA, Cowie CT, Janev O, Whitfield CR et al (2023) The health effects of 72 hours of simulated wind turbine infrasound: a double-blind randomized crossover study in noise-sensitive, healthy adults. *Environ Health Perspect* 131(3):037012
- Mayr S, Burkhardt H (2005) Ultrasonic properties of sedimentary rocks: effect of pressure, saturation, frequency and microcracks. *Geophys J Int* 164(246–258):12. <https://doi.org/10.1111/j.1365-246X.2005.02826.x>
- Met Office. (2010 - 2015) Cartopy: a cartographic python library with a Matplotlib interface. Exeter, Devon. <https://scitools.org.uk/cartopy>

- Nagel S, Zieger T, Luhmann B, Knödel P, Ritter J, Ummenhofer T (2021) Ground motions induced by wind turbines. *Civil Engineering Design* 3:73–86
- Neuffer T, Kremers S (2017) How wind turbines affect the performance of seismic monitoring stations and networks. *Geophys J Int* 211(3):1319–1327
- Neuffer T, Kremers S, Fritschen R (2019) Characterization of seismic signals induced by the operation of wind turbines in North Rhine-Westphalia (NRW) Germany. *J Seismol* 23(5):1161–1177
- Neuffer T, Kremers S, Meckbach P, Mistler M (2021) Characterization of the seismic wave field radiated by a wind turbine. *J Seismol* 1–20
- Pilger C, Ceranna L (2017) The influence of periodic wind turbine noise on infrasound array measurements. *J Sound Vib* 388:188–200
- Pohl J, Gabriel J, Hübner G (2018) Understanding stress effects of wind turbine noise—the integrated approach. *Energy Policy* 112:119–128
- Saccorotti G, Piccinini D, Cauchie L, Fiori I (2011) Seismic noise by wind farms: a case study from the virgo gravitational wave observatory, Italy. *Bull Seismol Soc Am* 101(2):568–578
- Schön J (1996) *Physical properties of rocks: fundamentals and principles of petrophysics*. Pergamon Oxford, OX, UK; Tarrytown, NY, USA ISBN 0080410081
- Stammler K, Ceranna L (2016) Influence of wind turbines on seismic records of the Gräfenberg array. *Seismol Res Lett* 87(5):1075–1081
- Tiab D, Donaldson EC (2016) Chapter 2 - introduction to petroleum geology. In Tiab D, Donaldson EC (eds) *Petrophysics (Fourth Edition)*, Gulf Professional Publishing, Boston, fourth edition pp 23–66 ISBN 978-0-12-803188-9. <https://doi.org/10.1016/B978-0-12-803188-9.00002-4>, <https://www.sciencedirect.com/science/article/pii/B9780128031889000024>
- Umit R, Schaffer LM (2022) Wind turbines, public acceptance, and electoral outcomes. *Swiss Political Sci Review* 28(4):712–727
- Zieger T, Ritter JR (2018) Influence of wind turbines on seismic stations in the upper rhine graben, SW Germany. *J Seismolog* 22(1):105–122
- Zieger T, Nagel S, Lutzmann P, Kaufmann I, Ritter J, Ummenhofer T, Knödel P, Fischer P (2020) Simultaneous identification of wind turbine vibrations by using seismic data, elastic modeling and laser doppler vibrometry. *Wind Energy* 23(4):1145–1153

Publisher's Note Springer Nature remains neutral with regard to jurisdictional claims in published maps and institutional affiliations.